ACSNANO

www.acsnano.org

ARTICLE

Rapid Fabrication by Lyotropic Self-Assembly of Thin Nanofiltration Membranes with Uniform 1 Nanometer Pores

Yizhou Zhang, Ruiqi Dong, Uri R. Gabinet, Ryan Poling-Skutvik, Na Kyung Kim, Changyeon Lee, Omar Q. Imran, Xunda Feng, and Chinedum O. Osuji*

Cite This: https://doi.org/10.1021/acsnano.1c00722

Read Online

ACCESS | Metrics & More | Article Recommendations | Supporting Information

ABSTRACT: Nanostructured materials with precisely defined and water-bicontinuous 1-nm-scale pores are highly sought after as advanced materials for next-generation nanofiltration membranes. While several self-assembled systems appear to satisfy this need, straightforward fabrication of such materials as submicron films with high-fidelity retention of their ordered nanostructure represents a nontrivial challenge. We report the development of a lyotropic liquid crystal mesophase that addresses the aforementioned issue. Films as thin as ∼200 nm are prepared on conventional support membranes using solution-based methods. Within these films, the system is composed of a hexagonally ordered array of ∼3 nm diameter cylinders of cross-linked polymer, embedded in an aqueous medium. The cylinders are uniformly oriented in the plane of the film, providing a transport-limiting dimension of ∼1 nm, associated with the space between the outer surfaces of nearest-neighbor cylinders. These membranes exhibit molecular weight cutoffs of ∼300 Da for organic solutes and are effective in rejecting dissolved salts, and in particular, divalent species, while exhibiting water permeabilities that rival or exceed current state-of-the-art commercial nanofiltration membranes. These materials have the ability to address a broad range of nanofiltration applications, while structure−property considerations suggest several avenues for potential performance improvements.

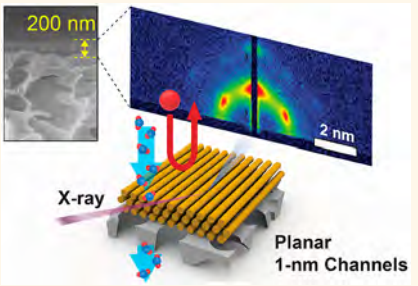

KEYWORDS: *self-assembly, nanofiltration, liquid-crystal membranes, lyotropic mesophase, nanochannel, thin film, desalination*

Nanofiltration (NF) membranes are increasingly important for water purification in diverse contexts including the remediation of industrial wastewaters and the removal of micropollutants in point-of-use applications.[1−3] They function by leveraging size-exclusion, solution diffusion, and electrostatic interaction phenomena to regulate solute transport and achieve desired separations.[4−6] In this regard, the precise fabrication of ordered single-nanometer water channels from molecular level design is one of the strategies to effectively regulate transport across the membrane.

Current NF membranes predominantly utilize loosely cross-linked polyamide networks or nanoporous polymers as the selective layer. In the first case, interfacial polymerization provides a thin film that separates solutes by a combination of steric hindrance, solution diffusion, and electrostatic interactions.[7] Such membranes are used in the majority of NF applications (*e.g.*, water softening) and reliably separate dissolved salts and molecular solutes at the 1 nm length scale. In the second case, a random network of nanopores formed by phase inversion can provide separation at the 1−2 nm length scale typically by a combination of size-exclusion and electrostatic interactions.[8,9] In both cases, the performance of such NF membranes suffers from the convolution of their selectivity with their permeability due to the random nature of the transport-regulating features in the system: the contorted molecular structure and multiscale heterogeneity induced by uncontrolled diffusion during fast interfacial polymerization in the first case[10−12] and the tortuosity and broad dispersion of pore sizes in the second case.[13] The resulting permeability−selectivity trade-off in conventionally fabricated membranes is an intrinsic property that represents a critical barrier to improving performance to address emerging challenges in water purification.[14−17]

Overcoming the permeability−selectivity trade-off and thereby realizing the next-generation of NF membranes calls

Received: January 26, 2021
Accepted: March 12, 2021

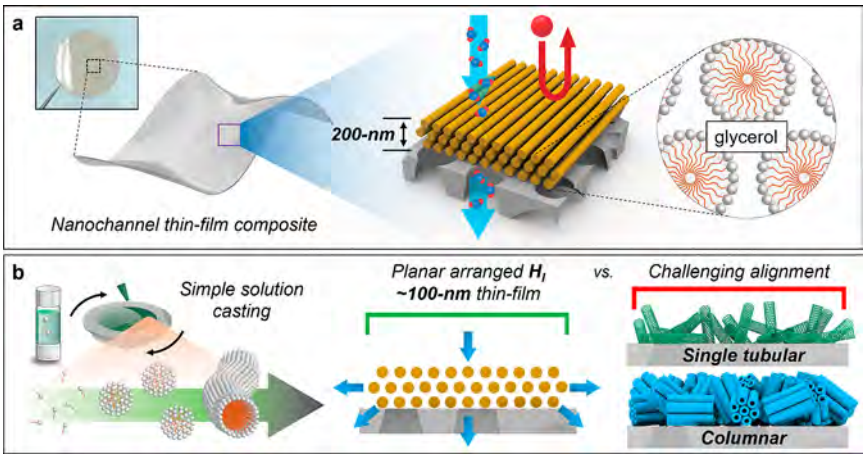

Figure 1. Nanostructured thin-film composite membrane derived from a lyotropic mesophase. (a) Schematic demonstrating the ordered cylindrical nanofibrils that provide transport-limiting features for molecular separation. The lyotropic mesophase is processed to yield a thin yet defect-free film composed of arrays of single-nanometer water-bicontinuous channels. Inset photograph: a 1-in.-diameter piece of a thin-film composite nanofiltration membrane. (b) The assembly of the lyotropic H_I begins with spin-coating a dilute solution of mesophase precursors dissolved in the selected organic solvent. Given a sufficient evaporation time, a critically low concentration of volatile solvent allows for microphase separation that leads to an ultrathin film of direct cylindrical mesophase planar arranged at the equilibrium. The water-bicontinuous structure provided more efficient transport relative to transport within cylindrical nanopores, depicted on the right.

for rational design that better separates the axes controlling selectivity and permeability. Recent efforts include consideration of molecularly designed framework systems such as COFs,[18,19] MOFs,[20,21] and polymers of intrinsic microporosity,[22,23] the assembly of discrete water-transporting nanostructures, synthetic and natural, such as CNTs,[24,25] AQPs,[26,27] and graphenes,[28,29] and the self-assembly of nanostructured materials such as liquid crystals (LC)[30−33] and surfactants.[34−36] In terms of materials engineering, the strategy underpinning such efforts is the precise definition of the size of transport-regulating features and the interactions of such features with solutes to govern the selectivity of the system. The number density of the structures thereafter dictates the *intrinsic* property of the material, *i.e.*, its *permeability* (typically denoted in L m^{-2} h^{-1} bar^{-1} μm), which in turn dictates the overall *flux* of fluid through the membrane in operation. At the device level, minimizing the thickness of the membrane provides an important second means of maximizing flux by optimizing the *extrinsic* property, the membrane *permeance* (typically denoted in L m^{-2} h^{-1} bar^{-1}), to first order, independent of selectivity. Such modification of performance by minimizing thickness has emerged as a viable concept in the context of conventional polyamide membranes, for example, by preparing sub-10 nm polyamide films.[37,38] However, while it is simple to conceptualize the fabrication of very thin membranes to improve flux, as a practical matter, the preparation of such materials without defects in device-relevant geometries (*i.e.*, on mechanical supports) over practically useful dimensions (>1 cm^2) represents a decidedly nontrivial challenge. Overcoming this challenge requires knowledge and manipulation of the relevant structure−property relationships and optimization of material compositions and processing methods.

Next-generation NF membranes therefore demand the fabrication of thin materials that feature strictly defined 1−2-nm-scale continuous channels from tailor-made molecular building blocks.[39,40] Self-assembly of various small-molecule systems (molar mass ~200−800 Da) can provide access to such features, yielding transport-regulating nanostructures that are highly ordered with characteristic dimensions that are thermodynamically governed. Considerable attention has been given in particular to the use of self-assembled LC mesophases.[41,42] Here, sieving by transport within discrete cylindrical pores of hexagonal columnar systems or within the bicontinuous pores of cubic gyroid mesophases has been targeted.

Work by Gin and co-workers successfully demonstrated the formation of membranes from a polymerized bicontinuous cubic lyotropic mesophase (Q_I) formed by gemini surfactants. The membranes demonstrated a high selectivity for solutes smaller than 0.9 nm, but the thick films (~3 μm) limited the hydraulic permeance to less than 0.02 L m^{-2} h^{-1} bar^{-1}.[36] More recently, Sakamoto *et al.* reported data on wedge-shaped aromatic moieties that formed hexagonal columnar (Col_h) and bicontinuous cubic (Cub_{bi}) mesophases.[43] The Cub_{bi} membranes rejected ~30% of raffinose (1.2 nm). By comparison, the Col_h membranes demonstrated 72% raffinose rejection. While the orientation of the columnar nanopores was not controlled to optimize the permeability, these membranes nonetheless demonstrated a relatively high hydraulic permeance of ~1.2 L m^{-2} h^{-1} bar^{-1} in NaCl solution due to the small thickness (*ca.* ~100 nm) of the self-assembled selective layer. By contrast, commercial NF membranes provide a permeance of ~10 L m^{-2} h^{-1} bar^{-1} and are capable in some cases of separating ions in solution.[44] It is therefore apparent that while NF membranes based on self-assembled materials hold considerable potential, significant challenges to realizing this potential remain. In particular, there are severe technical and scientific challenges associated with ensuring appropriate organization of self-assembled transport regulating nanostructures in thin films on suitable mechanical supports, while consistently preserving the physical integrity of such films to make them viable as NF membranes.[34]

Here, we present a system that overcomes the above-mentioned challenges by enabling the fabrication of thin (<500 nm) yet defect-free films with continuous solvent-accessible transport pathways (Figure 1). The system is composed of a glycerol-based mixture (the glycerol contains 10 wt % water)

https://doi.org/10.1021/acsnano.1c00722
ACS Nano XXXX, XXX, XXX−XXX

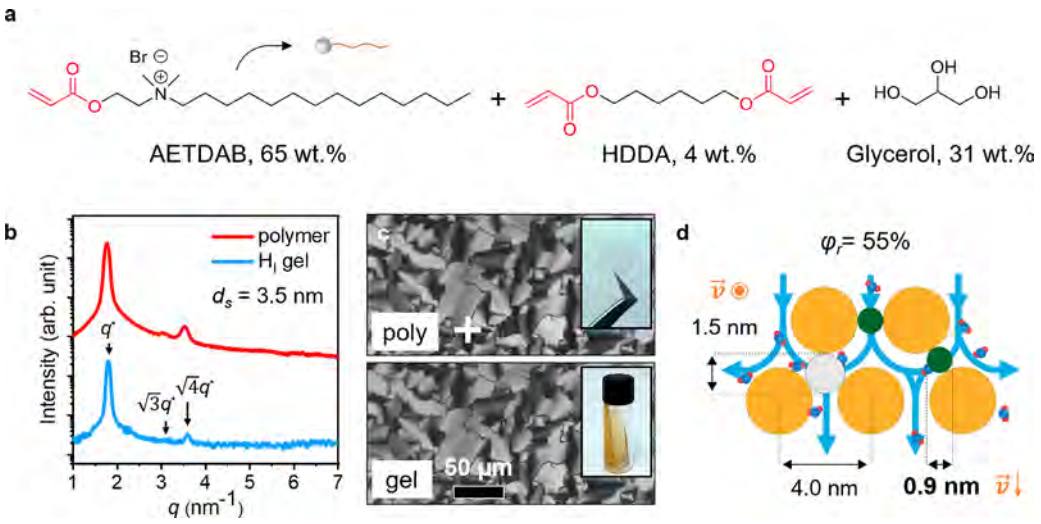

Figure 2. Structural analysis demonstrates high-fidelity retention of the H_I mesophase with a 1 nm separation feature. (a) Molecular structure of the lyotropic precursor that self-assembles into the mesophase at equilibrium. The mesophase is composed of the polymerizable amphiphilic acrylate AETDAB, the hydrophobic cross-linker hexanediol diacrylate (HDDA), and aqueous content glycerol. (b) 1D SAXS data demonstrate the comprehensive retention of a nanostructured template from a lyotropic mesophase during the photoinitiated cross-linking in bulk. A consistent characteristic q ratio is maintained with an averaged center−center distance alternating from ∼3.6 to 3.5 nm. (c) From high-magnification polarized optical micrographs, identical birefringence texture was established. Micrographs were taken from a bulk sample prior to and after the cross-linking reaction. Inset: Photographs of the lyotropic gel and the free-standing polymeric thin film. (d) Schematic of an array of hexagonally packed nanofibrils that constructs the water-bicontinuous nanochannels available for nanofiltration. Assuming a cylinder volume fraction of 55%, planar ordered nanochannels provide solute separation at a 0.9 nm scale (labeled by the green circle), instead of the larger liming dimension of 1.5 nm (labeled by the gray circle).

of a cross-linker with a polymerizable cationic surfactant [2-(acryloyloxy)ethyl]dimethyl tetradecyl ammonium bromide (AETDAB), shown in Figure 2a. The mixture self-assembles to form hexagonally packed cylinders in an aqueous-continuous matrix that provides a highly ordered medium for nanofiltration with slit-shaped pores featuring critical dimensions of ∼1 nm. Whereas prior work in a water-based system relied on a dual cross-linker strategy (internal/external to the cylinders) using a methacrylate-based species,[34] our work here in a glycerol system utilized a single cross-linker and an acrylate-based species. The switch to an acrylate surfactant was driven by the suppression of the H_I mesophase of the methacrylate system at room temperature in the presence of glycerol. The mechanical reinforcement contributed by the use of an external cross-linker was found to be unnecessary in the current system, which simplified the formulation of the mesophase. Photoinduced cross-linking of the cylinders provides mechanical integrity and ensures that flow in the continuum around the cylinders is the dominant mode of transport. As a result, orientational control of the nanostructure is not required to guarantee effective fluid permeation. This is in contrast to systems with tubular nanopores such as inverse hexagonal (H_{II}) mesophases[45] or carbon nanotubes,[46,47] where the alignment of such structures presents a considerable challenge to realizing practically useful membranes. Intriguingly, the self-assembly of the mesophase in thin films yields uniformly planar orientations of the hexagonally packed cylinders, which is expected to display a lower critical dimension for transport regulation, relative to nonplanar or perpendicular oriented cylinders. Controlled deposition of films with thicknesses on the order of ∼100 nm on microporous mechanical supports yields thin-film composite (TFC) membranes. At ∼10 L m^{-2} h^{-1} bar^{-1}, the permeance of these TFC membranes rivals and in some cases exceeds the permeance of high-performance commercial nanofiltration membranes. Pressure-driven permeation data indicate that the critical effective pore size is *ca.* 1 nm based on the retention of charge-neutral solutes. Charged species are retained at even smaller dimensions due to electrostatic interactions with the positively charged nanostructures in the membrane. The low volatility of glycerol and the solubility of the system in several common solvents enable rapid and relatively simple fabrication of defect-free membranes using standard solution-based processing, in this case, spin-coating. While it was not the focus here, such techniques can be readily ported over to high-throughput manufacturing using roll-to-roll solution processing. In total, the system displays considerable potential for large-scale fabrication of next-generation nanofiltration membranes with well-defined nanostructures.

RESULTS AND DISCUSSION

Preserving Mesophase Order in Cross-Linked Thin Films. Successful membrane fabrication relies on the preservation of the H_I mesophase structure during processing. Avoiding potential changes in structure during film formation requires the use of nonvolatile components. For this reason, the lyotropic mesophase is constituted using glycerol (vapor pressure <1 Torr at 20 °C), instead of water (vapor pressure ∼20 Torr at 20 °C), and the composition was optimized to avoid phase changes during photoinduced cross-linking. AETAB was synthesized using a single-step Menshutkin reaction as detailed in Figure S1, Supporting Information. The optimized system was composed of 31 wt % glycerol, 4 wt % hexanediol diacrylate (HDDA), and 65 wt % AETAB. The self-assembly of the lyotropic H_I mesophase is evidenced by 1-D integrated small-angle X-ray scattering (SAXS) data coupled with polarized optical microscopy (POM), shown in Figure 2. Bulk film samples for optical characterization were prepared by

https://doi.org/10.1021/acsnano.1c00722
ACS Nano XXXX, XXX, XXX−XXX

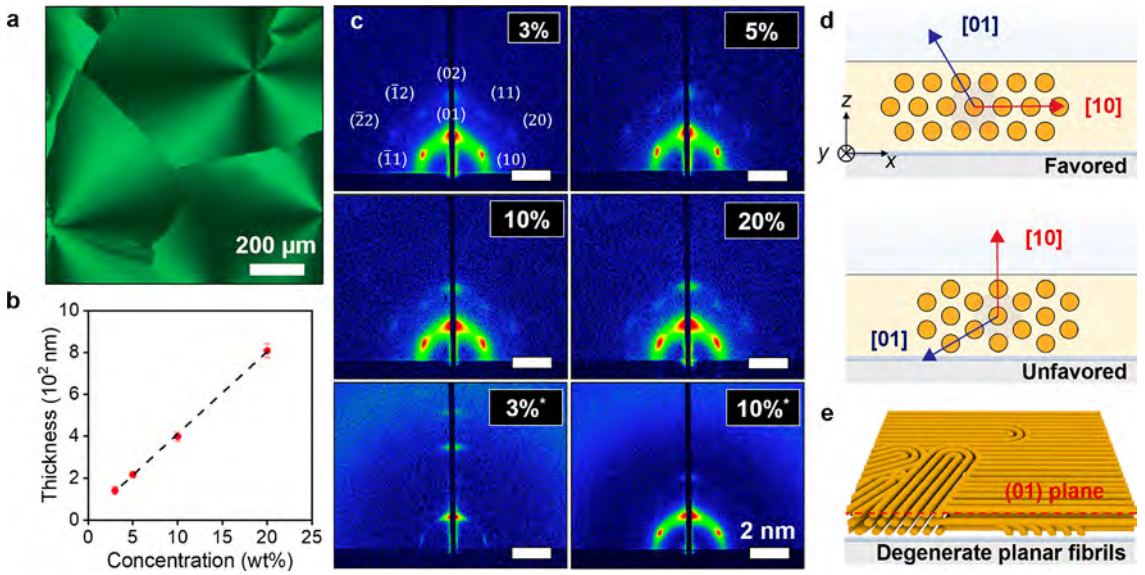

Figure 3. Thin films fabricated from spin-coating with preserved H_I nanostructure arranged with a degenerate planar alignment relative to the substrate. (a) Polarized optical micrograph of the cross-linked mesophase showing the retention of the mesophase order. (b) AFM-determined spin-coated film thicknesses on silicon substrates as a function of mesophase solution concentration. (c) Representative 2-D GISAXS patterns recorded from H_I thin films cast on bare and PVP-modified (*) silicon wafers from a range of mesophase solution concentrations from 3 to 20 wt %. The scattering pattern indicates that the cylinders lie parallel to the substrate. The 3 wt % sample on the PVP-modified surface undergoes a transformation to an apparent lamellar phase or a combination of lamellae and cylinders. (d, e) Schematic representations of the hexagonally packed cylinder nanostructure in which mechanical integrity originates in part from the physical interconnection of cylinders due to topological defects. The planar orientation and hexagonal lattice vector direction indicated by the GISAXS data are shown schematically.

mechanically pressing samples between glass slides and thermally annealing them to allow the birefringent texture to develop slowly. SAXS data (Figure 2b) show Bragg peaks from the ordered mesophase occurring at scattering wavevectors q relative to the principal Bragg reflection at q^* at ratios $(q/q^*)^2$ = 1, 3, and 4. This is consistent with the formation of hexagonally packed cylinders, which are also indicated from the fan-like texture observed in POM images (Figure 2c). The efficacy of cross-linking is demonstrated by FTIR spectra and the mechanical integrity analysis of the produced films (Figures S2 and S3, Supporting Information). It should be noted that the cross-linked cylindrical nanostructures do not fall apart in excess water. The nanostructures are interconnected and physically interlocked due to topological defects. Additionally, prior work has speculated that despite not being favored by solubility, there is a small but potentially important concentration of cross-links between cylinders that occurs during polymerization even in the absence of added external cross-linkers.[34] Retention of the hexagonal structure is indicated by the retention of the fan-like texture in POM and the Bragg reflections in SAXS taken from the sample after photo-cross-linking (details in Figures S4 and S5, Supporting Information). The concentration of photoinitiator (2-methoxy-2-phenylacetophenone) added for this purpose was optimized at 0.04 wt %.

SAXS data (Figure 2b) reveal a small change of roughly 3% in the d-spacing on photo-cross-linking, from 3.6 to 3.5 nm. Assuming that the Br^- counterion resides in the fluid phase, and similar mass densities for the discrete and continuous phases, the volume fraction of the cylinders is estimated at φ_r = 0.55. On this basis, the critical dimensions for transport perpendicular and parallel to the cylinder long axes are 0.9 and 1.5 nm, respectively, as shown in Figure 2d. These dimensions represent the largest circular cross sections that can travel unimpeded by the cylinders in the given directions. Additional details regarding the calculation of these dimensions is provided in Figure S6, Supporting Information. A selective layer composed of all planar-oriented cylinders therefore is more restrictive than one in which the cylinders are oriented normal to the film surface.

Structural Characterization. Solutions of the mesophase were prepared in ethyl acetate (vapor pressure ~70 Torr at 20 °C) at various concentrations and spin-coated at 2000 rpm onto polished (100) silicon substrates to prepare films for structural characterization shown in Figure 3. The resulting samples were allowed to sit quiescently under ambient conditions for 2 min to ensure complete solvent evaporation and mesophase assembly, before subsequent photo-cross-linking. The thicknesses of the resulting thin solid films were characterized using height profiles measured by atomic force microscopy (AFM). As shown in Figure 3b, there was a linear correlation between the solution concentration and the resulting film thickness.

Two-dimensional grazing-incidence small-angle X-ray scattering (GISAXS) was used to provide information regarding the in-plane morphology in the films. GISAXS patterns of films deposited from solutions ranging from 3 to 20 wt % consistently demonstrate a well-resolved pattern of sharp hexagonally arranged Bragg spots, as shown in Figure 3c. The primary reflection occurs at a consistent d-spacing of 3.5 nm independent of film thickness. The occurrence of the (01) and (02) reflections (*i.e.*, $(10\bar{1}0)$and $(20\bar{2}0)$ reflections, in 4-index notation) along the specular line (*i.e.*, the z-direction or the film normal) indicates that the hexagonally packed cylinders lie in the plane of the film. That is, the long axes of the cylinders lie in the $x-y$ plane. This represents a degenerate situation

https://doi.org/10.1021/acsnano.1c00722
ACS Nano XXXX, XXX, XXX−XXX

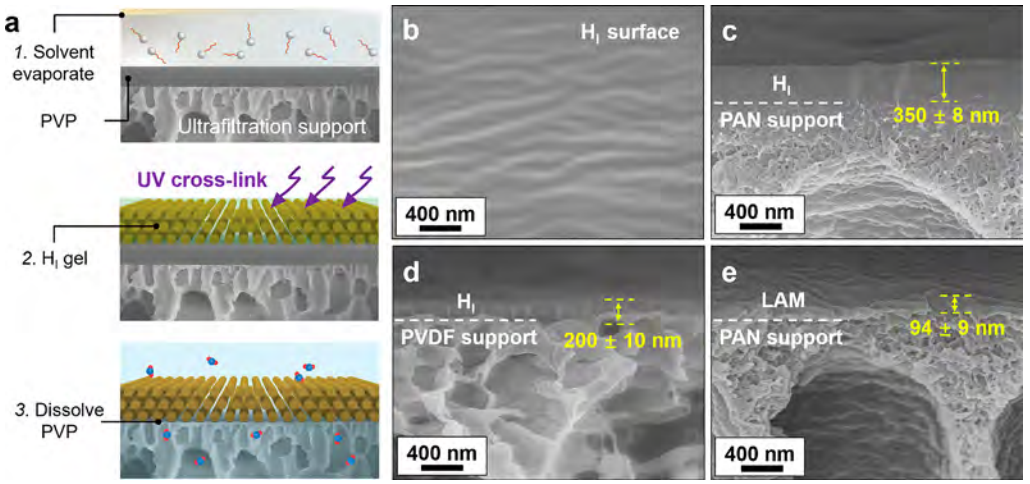

Figure 4. Schematic of the composite membrane fabrication with corresponding micrograph analysis. (a) Sacrificial layer assisted fabrication protocol based on spin-coating generates ultrathin TFC membranes without significant solution infiltration. (b) The surface micrograph for H_I TFC possesses a rather smooth surface. The membrane was cast from spin-coating a 10 wt % H_I solution dissolved in ethyl acetate on polyacrylonitrile (PAN) covered with PVP, with subsequent UV cross-linking. (c) A thin-film mesophase template with homogeneous cross-section was generated after rinsing the water-soluble protective layer from the PAN-H_I. (d) Casting the same mesophase solution formulation on a PVP/polyvinylidene fluoride (PVDF) composite results in a lower film thickness. The PVDF-supported H_I-TFC membrane demonstrates a hydraulic permeance of 10 L m^{-2} h^{-1} bar^{-1}, which is comparable with high-performance nanofiltration membranes. (e) Ultrathin lamellar (LAM) film fabricated from casting a 3 wt % solution on sacrificial layer protected PAN.

however as the cylinders are free to explore all orientations within the plane, and it is this degeneracy that gives rise to the asymmetry in the intensity of the Bragg reflections, with higher intensity observed for the (01) spot along the specular line, compared with that of the off-specular (10) and ($\bar{1}$1) spots. Further, the orientation of the scattering pattern indicates that the system selects a specific lattice orientation relative to the film surface, with the [10] direction, *i.e.*, the direction along which the cylinders are close-packed, in the plane of the film ((10$\bar{1}$0) planes parallel to the film surface). Similar lattice orientations have been observed in block copolymer films[48,49] and lyotropic mesophases textured by shear flow.[50] Anisotropy of lattice orientation may also be expected due to commensurability constraints in situations where the film thickness is comparable to the lattice parameter. In the present case, commensurability is an unlikely explanation given the large thickness of the films (~30−200 lattice units). We surmise that the observed orientation may originate due to shear experienced during spin coating, potentially due to rapid solvent evaporation or to a still unidentified surface phenomenon. In contrast, bulk samples do not show preferred orientation (Figure S7, Supporting Information).

Subsequent fabrication of thin-film composite membranes involved spin-coating on porous polymer supports bearing a sacrificial layer of poly(vinylpyrrolidone) (PVP). We therefore examined the morphology of mesophases deposited on PVP-coated silicon substrates. PVP is insoluble in the spin-coating solvent, ethyl acetate, but is soluble in water, and therefore acts as an effective sacrificial layer enabling the rapid fabrication of membranes by spin-coating. Thin films were prepared on PVP from 3 and 10 wt % solutions. GISAXS data (Figure 3c) reveal that for the ~100-nm-thick film prepared from a 3 wt % solution the system transitioned from hexagonally packed planar cylinders to planar lamellae. The lamellar (LAM) morphology is confirmed by the 1D azimuthally averaged data (Figure S8, Supporting Information). Conversely, the ~350-nm-thick film prepared from the 10 wt % solution maintained the display of planar cylinders with the (10$\bar{1}$0) in the plane of the film, as seen earlier for films prepared directly on silicon. We speculate that the structural transformation to lamellae is driven by a shift in the system composition due to the small uptake of glycerol (or water from the glycerol) by the PVP substrate. Taking the relevant mass balances into consideration, it is apparent that this effect can be mitigated by modifying the thickness of the PVP layer relative to the deposited mesophase or post-treating the PVP to prevent absorption of even small amounts of glycerol. For simplicity, all membrane fabrications were subsequently conducted using 10 wt % solutions.

Fabricating Thin-Film Composite Membranes. High hydraulic permeance is important for practical utility as a nanofiltration membrane. While it is possible to fabricate composite membranes by directly coating porous ultrafiltration mechanical supports with our mesophase, the hydraulic resistance that results from clogging of the support with the mesophase produced an unsatisfactory permeance of <1 L m^{-2} h^{-1} bar^{-1}. The earlier described sacrificial layer strategy was developed to circumvent this issue. As schematically illustrated in Figure 4a, the strategy entails the use of a dense, smooth polymer layer with orthogonal solubility relative to the mesophase. PVP was chosen for this purpose, and deposition was conducted by spin-coating. Two microporous ultrafiltration membranes were explored as mechanical supports for thin H_I membranes, *viz.*, poly(acrylonitrile) (PAN, Snyder PX) and polyvinylidene fluoride (PVDF, Snyder V6), here defined as PAN-H_I and PVDF-H_I, respectively. SEM images of the support membranes are provided in Figure S9, Supporting Information. The sacrificial layer strategy resulted in the fabrication of composite membranes with significantly higher permeances of ~10 L m^{-2} h^{-1} bar^{-1} (see Figure S10, Supporting Information).

The ability to fabricate thin-film composite membranes using the mesophase and the sacrificial layer strategy is demonstrated by the SEM images in Figure 4. The

https://doi.org/10.1021/acsnano.1c00722
ACS Nano XXXX, XXX, XXX−XXX

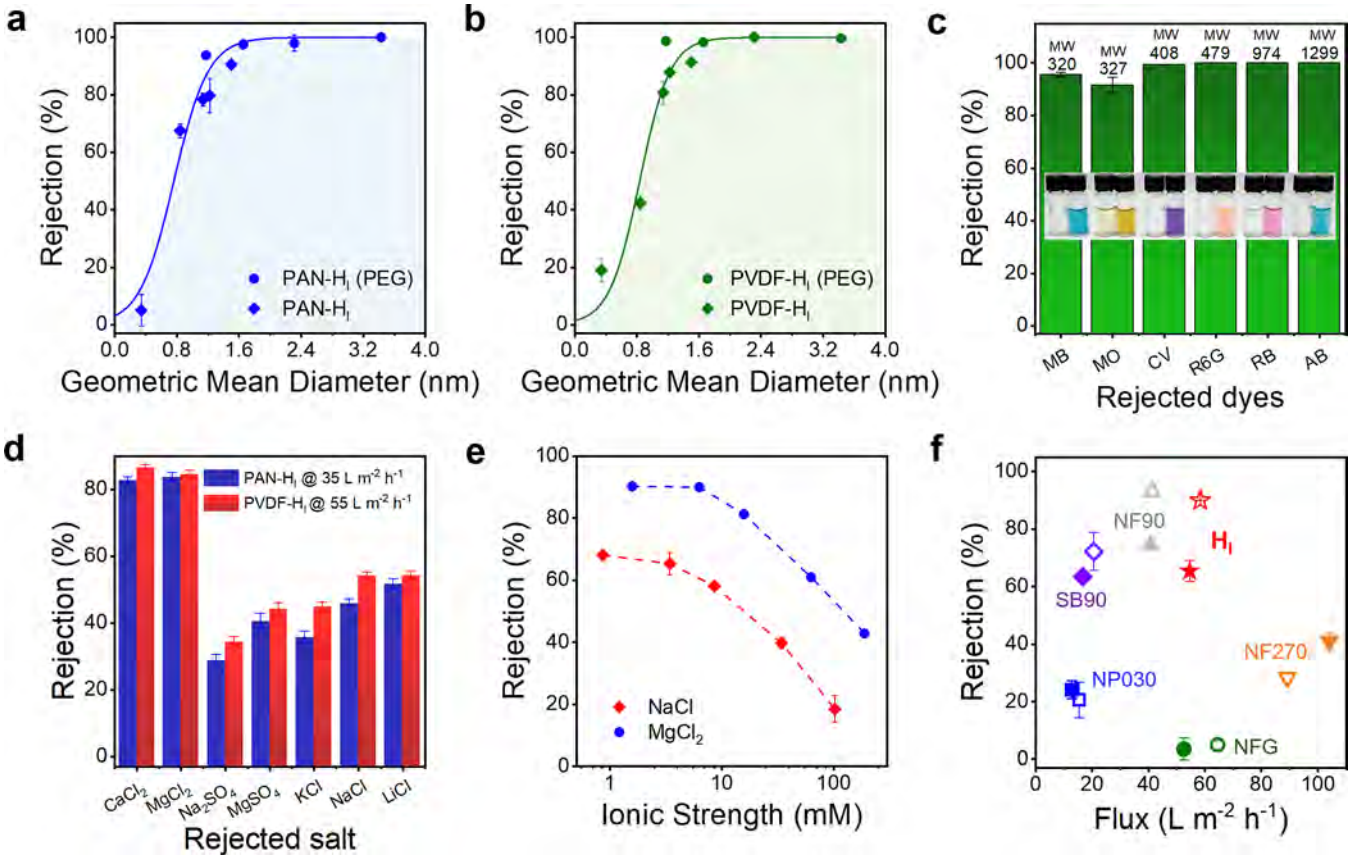

Figure 5. Solute separation performance of the thin lyotropic liquid crystal membranes based on cross-linked mesophases. Size-selective solute rejection curves displayed a 1 nm critical dimension for (a) PAN-H$_I$ and (b) PVDF-H$_I$. The rejection experiment was executed based on measuring the passage of a single neutral solute with known sizes including polyethylene glycols (PEG) and irregularly shaped small molecules. (c) Exemplary rejection experiment illustrating the ubiquitous charged molecule purification capability of the cross-linked mesophases. Inset: Photograph for the clear dye solution after the filtration contrast clearly with the feed, taken from the rejection experiment of PAN-H$_I$. (d) Survey of salt rejection to investigate the ionic separation functionality of the H$_I$ membranes. The salt solutions selected have different ion valence ratios from counterions and co-ions, but a consistent ionic strength at 10 mM. (e) Ion rejection performance as a function of salt solution concentration using NaCl and MgCl$_2$ as model solutes. An induced electrostatic screening with increasing ionic strength lowered the extent of rejection. (f) Quantitative performance evaluation of PVDF-H$_I$ TFC compared to other commercially available nanofiltration membranes, using feed solutions containing 200 ppm of NaCl (solid symbols) or MgCl$_2$ (hollow symbols) as model solutes.

micrographs were taken after the membranes were rinsed to remove PVP. They show smooth photo-cross-linked selective layers, sitting conformally on top of microporous PVDF and PAN support membranes. The surface morphology of a composite membrane prepared by coating a 10 wt % mesophase solution onto PVP-modified PAN is shown in Figure 4b. The cross-sectional view of the same composite membrane in Figure 4c shows a ~350 nm thick H$_I$ selective layer along with the underlying PAN ultrafiltration support. This PAN-H$_I$ membrane possesses a hydraulic permeance of 6.1 L m^{-2} h^{-1} bar^{-1} and therefore a permeability of ~2 L m^{-2} h^{-1} bar^{-1} μm. The measured permeability is in good agreement with the theoretical estimate of the permeability expected for this membrane, as detailed in calculations in the Supporting Information.[51] By comparison, a thinner selective layer of ~200 nm formed on modified PVDF (Figure 4d) exhibits a higher permeance of 10.0 L m^{-2} h^{-1} bar^{-1}. The inferred permeability at ~2 L m^{-2} h^{-1} bar^{-1} μm is in line with the prior mentioned theoretical estimate. The composite H$_I$ membranes were resilient to pressure-driven flow and to shear induced by the stirring used during the transport characterization, where no occurrence of film delamination nor change in membrane permeance and solute rejection was observed after the complete removal of the sacrificial layer.

Solute rejection measurements were conducted to elucidate the size-selectivity of the membranes. Membranes were challenged with polyethylene glycol (PEG) of varying molar masses and a series of small neutral molecules with sizes ranging from ~0.3 to 3 nm, *viz.*, resorcinol, vitamin B2, vitamin B12, and alpha- and beta-cyclodextrin. The hydrodynamic diameter of the PEG and principal diameters of the cyclodextrins were sourced from prior literature.[52−55] Meanwhile, the geometric mean sizes of other solutes were determined from spatial dimensions calculated using the Chem3D software package represented by the geometric mean diameter, $d_m = (d_1 d_2 d_3)^{1/3}$, where d_1, d_2, and d_3 are the dimensions of the molecule along its principal axes. The effective sizes of the molecular solutes are detailed in Figure S11, Supporting Information. The extent of rejection, R, was calculated by comparing the concentration of the solute in the feed solution to the concentration measured from the permeate at steady state, with $R = \left(1 - \frac{C_p}{C_f}\right) \times 100\%$, and were corrected for the effects of concentration polarization.[56]

https://doi.org/10.1021/acsnano.1c00722
ACS Nano XXXX, XXX, XXX−XXX

The data are summarized in rejection curves shown in Figure 5a and b. Note that while there are analytical theories and accompanying closed form expressions for the partitioning (and therefore the rejection) of spherical solutes from cylindrical pores, no such theory is available to describe solute partitioning in the interstitial space surrounding ordered, densely packed slender cylinders. Nevertheless, based on empirical data for transport in disordered packings of fibrillar elements,[57] we anticipate a sigmoidal evolution of rejection from 0 to 100% for this system. The rejection data for PEG and for the neutral solutes were therefore collectively fit using a logistic function (details in Supporting Information) to provide a reasonable representation of the rejection characteristics of our membranes. On this basis, we estimated the size cutoff, *i.e.*, the solute size corresponding to a rejection of 90%, for our membranes. Membranes fabricated on PAN and PVDF display similar characteristics, with a cutoff at 1.2 nm. For solutes such as neutral density globular proteins, this cutoff corresponds to a molecular weight cutoff (MWCO) of roughly 600 g mol^{-1}.

Molecular Solute and Ion Transport through Nanostructured Films. The solute rejection data indicate the membranes have a higher selectivity (*i.e.*, larger rejection) for the polymeric solute, PEG, than for other similarly sized but nonpolymeric neutral molecular species. The membranes almost completely rejected the smallest PEG (600 g mol^{-1}) with a hydrodynamic diameter of ~1.2 nm with H_I-PVDF (R = 99%) and H_I-PAN (R = 94%), respectively. By contrast, the rejection of 1100 g·mol^{-1} beta-cyclodextrin with a geometric mean diameter of 1.2 nm was markedly lower, with R = 88% for the PVDF-supported membrane and R = 80% for the PAN-supported membrane, suggesting the beta-cyclodextrin travels 3 to 9 times faster than the 600 g mol^{-1} PEG across the membranes. We speculate that this difference in solute rejection is due to the shape anisotropy of both the solute and the channels through which transport occurs. For planar cylinders, transport occurs through the slit-like channels between the cylinders. As such, while the geometric-mean diameter for a solute may exceed the spacing between cylinders, the passage of such a solute may still occur, albeit hindered, if at least one of the principal dimensions does not exceed this gap. Indeed, for all the solutes considered here, with the exception of vitamin B12, the size along the shortest principal axis is <0.9 nm, the gap between the cylinders. Conversely, for globular objects such as PEG chains in solution, we expect no such anisotropic effects. It is worth noting that for spherical solutes slit-like pores demonstrate superior selectivity, at equivalent permeability, relative to cylindrical pores.[58,59] This suggests a potential route to improved selectivity in nanofiltration applications using the currently developed system.

The preceding data demonstrate that the membranes are capable of efficiently separating neutral solutes with sizes of *ca.* 1 nm. For charged solutes, one anticipates additional selectivity based on electrostatic interactions, given the positive charge on the surfaces of the cross-linked cylinders. Data for the rejection of charged molecular dyes are shown in Figure 5c. The lowest rejection was encountered for the smaller of the two negatively charged species considered, methyl orange (R = 91%, 327 Da). For the larger anionic dye, Rose Bengal, complete rejection was observed. For positively charged dyes, rejection was above 95% in all cases, down to the smallest species considered (methylene blue, 320 Da). No significant reduction in the hydraulic permeance was observed during dye permeation throughout the weeks-long transport experiment, indicating the absence of molecular fouling and that the separation is unrelated to charged species adsorption within the membrane.

Data for the rejection of dissolved salts further elucidate the role of electrostatic interactions. Experiments were conducted using a variety of salts with complementary identities, at a fixed ionic strength (I) of 10 mM and transmembrane pressure of 5.5 bar. Data are shown in Figure 5d. We observe the largest rejections, above 80%, for salts of type $A^{2+}B_2^-$, *i.e.*, salts of divalent metal cations with monovalent anions ($CaCl_2$; $MgCl_2$). These rejections are considerably larger than those observed (~40−60%) for the chloride salts of monovalent cations. The difference may originate due to the larger size (diameter) of hydrated divalent cations ($d_{Mg^{2+}}$ = 0.85 nm; $d_{Ca^{2+}}$ = 0.82 nm) relative to monovalent species (d_{Li^+} = 0.76 nm; d_{Na^+} = 0.72 nm; d_{K^+} = 0.66 nm),[60] or to the increased strength of repulsive electrostatic interactions for divalent cations with the fixed positive charges on the membrane. Early ultrafiltration studies firmly established the strong role of electrostatics as they identified an increase in rejection with an increase of co-ion valency due to stronger repulsive electrostatic interactions; the comparatively large pore sizes in ultrafiltration (>5 nm) mean that steric interactions, *i.e.*, size-exclusion, was not factor in the selectivity.[61−63] In the present case, however, we cannot exclude a potential contribution from steric effects, given the ~1 nm length scale of transport-limiting features. Indeed, data for A^+B^- salts (KCl, NaCl, LiCl) suggest there is a small but observable contribution from steric effects even for the small monovalent species, as we observe a subtle but clear correlation, with rejection increasing with the size of the hydrated cation, d_{Li^+}(0.76 nm) > d_{Na^+}(0.72 nm) > d_{K^+}(0.66 nm). Finally, for salts of divalent anions, we observe intermediate rejections that reflect the decrease of co-ion repulsion from the membrane due to enhanced screening by adsorption of a divalent, rather than monovalent, counterion.[63−65] In this two-member series (Na_2SO_4; $MgSO_4$) we note the occurrence of higher rejection for the divalent co-ion salt compared to the monovalent one. To what extent this difference originates from stronger electrostatic interactions of the divalent cation with the membrane or from the larger size of the cation relative to the monovalent species is unclear. Experiments conducted as a function of ionic strength (Figure 5e) show a steady decrease of rejection on increasing salt concentration. The reduction in rejection on increasing ionic strength is in line with expectations based on the role of electrostatic interactions in the present system. Prior work in ultrafiltration membranes has been successful in using a continuum approach to account for the role of ionic strength in salt rejection, particularly at low ionic strengths where the electrical double layer is larger than the pore diameter.[63] A rigorous quantitative evaluation of salt rejection is precluded here however by the small pore size, for which continuum theory is ill suited.[25,66−69]

The performance of our mesophase-derived membranes was compared against five commercial nanofiltration membranes. Data were collected in-house under identical conditions for all membranes considered, *viz.*, 200 ppm of NaCl (I = 3.4 mM) and $MgCl_2$ (I = 6.3 mM) as model salts, with a transmembrane pressure of 5.5 bar. The resulting hydraulic flux, as well as the salt rejection, are shown in Figure 5f. The mesophase-derived TFC simultaneously demonstrates better

https://doi.org/10.1021/acsnano.1c00722
ACS Nano XXXX, XXX, XXX−XXX

flux and rejection than common asymmetric polymeric nanofiltration membranes such as cellulose acetate SB90 or poly(ether sulfone) NP030. In terms of rejection only, our TFC membrane shows similar performance to the most selective commercial membrane tested, NF90. The observed flux of 55 L m^{-2} h^{-1} exceeds the flux of NF90, as well as that for NFG, both examples of high-flux polyamide TFC membranes. While NF270 exhibits a roughly 2-fold flux, it has a lower permeability of 0.6 L m^{-2} h^{-1} bar^{-1} μm compared to the 2 L m^{-2} h^{-1} bar^{-1} μm of the mesophase membrane. It is conceivable that additional optimization to further decrease the thickness of the mesophase membrane will result in flux that is comparable to, or even exceeding, that of NF270. In total, the combined rejection and flux characteristics are generally superior to, or comparable with, the in-house performance of commercial nanofiltration membranes. Notably, this performance was recorded for relatively low pressure operation, which represents an attractive regime for point-of-use nanofiltration or otherwise low-intensity operations such as industrial wastewater remediation.

CONCLUSION

In conclusion, we demonstrated here ultrathin and defect-free direct columnar (H_I) mesophase membranes that can be prepared using a rapid solution processing approach. The well-defined, water-continuous structure results in hydraulic permeances similar to or higher than those displayed by current state-of-the-art high-performance commercial TFC membranes that rely on rather disordered polyamide networks as active layers. The solute rejection characteristics are consistent with a system that features a uniformly planar H_I orientation yielding a transport-limiting dimension of ~1 nm. The rejection of charged solutes and in particular subpore diameter salts highlights the significant contribution from electrostatic interactions due to the presence of quaternary ammonium species on the surfaces of the cross-linked polymer cylinders that compose the active layer. The nanostructure of membranes derived from these mesophases can be tailored in a rational manner through the molecular structure and mesophase composition, which dictate the limiting dimension and porosity of the system. We anticipate that the currently developed materials have the potential to address several applications in nanofiltration, in particular where high selectivity and permeability are required at modest operating pressures. Systematic examination of fouling by prevalent foulants and detailed process studies under different operating conditions will be needed to support any large-scale implementation of these membranes, however. Additionally, while the success of spin-coating fabrication points favorably toward eventual large-scale roll-to-roll solution-based fabrication, successful migration between these two processes will require associated optimizations of materials and methods.

METHODS

Synthesis of the Lyotropic Surfactant. All chemicals used in this study were purchased from Sigma-Aldrich and used as received unless otherwise noted. Ultrafiltration supports and commercially available nanofiltration membranes were purchased from the Sterlitech Corporation. The glycerol stock solution was prepared through mixing 90 wt % of ≥99.5% glycerol (Fisher Scientific, maximum water content 0.5%) with 10 wt % DI water (R = 18 MΩ cm). Solid photoinitiator 2-methoxy-2-phenylacetophenone (Acros Organics) was dissolved in a stock solution of HDDA (Alfa Aesar) at a concentration of 1 wt %.

The cationic surfactant (AETDAB) was synthesized using a single-step Menshukin reaction following previously reported protocols. Typically, a mixture of 2-(dimethylamino)ethyl acrylate (15 g, 0.1 mol), 1-bromotetradecane (32 g, 0.11 mol), and hydroquinone (0.6 g, 0.05 mol) was dissolved in 250 mL of a binary solvent composed by 50/50 (v/v) acetonitrile and tetrahydrofuran. Once a homogeneous mixture was acquired, the reactant solution was then transferred to a 500 mL reaction flask containing a magnetic Teflon stir bar. Subsequently, the flask was refilled with nitrogen and was stirred at 40 °C in an oil bath for 72 h. After this time, the orange-colored solution was allowed to cool to room temperature. Subsequently, the solid product was obtained from precipitating and rinsing the reaction mixture with an excessive amount of cold, anhydrous diethyl ether for at least three times. Finally, the product was dried under vacuum overnight. ^{1}H NMR spectra of the AETDAB was collected from a Bruker AVII 500 spectrometer using deuterated chloroform ($CDCl_3$) as the solvent.

Cross-Linking H_I Films for Nanostructural Characterizations. The self-assembled lyotropic H_I mesophase at bulk was prepared through mixing a ternary mixture of 65 wt % AETDAB, 31 wt % glycerol, and 4 wt % HDDA doped with the photoinitiator, by stirring a stainless steel syringe needle in the mixture coupled with centrifuge mixing (Eppendorf Minispin) until a homogeneous, lyotropic liquid-crystal mesophase was generated. In order to fabricate mesophase film at bulk, lyotropic gel samples were sandwiched between two sonication precleaned glass slides to confine a film thickness of *ca.* 100 μm.

Meanwhile, H_I thin films (*i.e.*, with thickness ≤1 μm) were cast from solutions of mesophase precursors dissolved in an organic solvent (*i.e.*, ethyl acetate) by spin-coating with a range of concentrations from 3 to 20 wt %. Thin films are supported by silicon wafers with one side exposed to the atmosphere. In this manner, ultrathin mesophase films were directly coated on the selected substrates at a spin speed of 2000 rpm for 1 min with predetermined concentrations. Thin films were prepared on both precleaned (100) silicon substrates and cleaned glass slides. In the latter portion of the study, in order to understand the phase behavior of thin films in the presence of modified substrate chemistry, silicon substrates were coated with a thin layer of PVP that resembles the sacrificial layer in the membrane fabrication procedure. To prepare the sacrificial layer, a 20 wt % 55 kg mol^{-1} PVP casting solution composed of 50/50 (w/w) water/ethanol was spin-coated on silicon substrates using a spin speed of 3000 rpm for 5 min. Further, in order to explore the phase behavior of the LC mesophase thin film during the cross-linking, 20 wt % mesophase dissolved in acetonitrile was spin-coated on glass slides with photoinitiator doping ranging from 0.04 to 1 wt %. Additionally, prior to cross-linking, the self-assembled mesophase films for optical analysis were subsequently annealed and slowly cooled to develop spherulites with cylinders tangentially arranged for enhanced visual contrast.

Finally, photoinitiated cross-linking of the mesophases was conducted through illuminating a focused UV beam (100-W Sunspot SM) with the spectra distribution covering a range of wavelengths from 275 to 450 nm on films at a distance of 8 cm under a N_2 atmosphere at room temperature for 25 min. The conversion of the photoinitiated cross-linking reaction at bulk was estimated from the Fourier transform infrared spectra (FTIR), which were collected from a Jasco FT/IR-6800 FTIR spectrometer over the range of wavenumbers from 300 ≤ ν ≤ 400 cm^{-1}.

Fabrication of H_I Thin-Film Composites. A sacrificial layer methodology is employed to build a dense, but water-soluble surface layer atop ultrafiltration supports before mesophase solution coating. With the sacrificial layer barrier, the potential solution infiltration into the support, which could lead to additional hydraulic resistance at the H_I–support interface, was prevented. Specifically, two ultrafiltration mesoporous membranes with different macromolecular chemistries and MWCO greater than 400 kg mol^{-1} were investigated as structural supports.

https://doi.org/10.1021/acsnano.1c00722
ACS Nano XXXX, XXX, XXX–XXX

PAN (MWCO 400 kg mol^{-1}, Synder PX) and PVDF (MWCO 500 kg mol^{-1}, Synder V6) ultrafiltration membranes were coated with a layer of water-soluble PVP thin film. The coating was conducted through spin-coating different PVP solutions at a consistent spin rate at 3000 rpm for 5 min. A casting solution consisting of 55 kg mol^{-1} PVP dissolved in 50/50 (w/w) water/ethanol was used for coating a PAN ultrafiltration support. Similarly, 12 wt % 360 kg mol^{-1} PVP dissolved in ethanol was coated on a PVDF support. Supports with sacrificial layers were dried under vacuum before immediate use in the following H_I composite membrane fabrication.

H_I composite membranes were prepared in a fume hood situated in an air-conditioned laboratory with a regulated temperature between 18 and 23 °C and relative humidity between 20% and 60%. The membrane casting solution was prepared through dissolving mesophase precursors in a solution of ethyl acetate at a concentration of 10 wt %. The homogeneous solution was filtered through a 0.2 μm polytetrafluoroethylene (PTFE) syringe filter and degassed before use. In order to cast a composite membrane, the mesophase solution was dropped on the selected support and was spin-coated at 2000 rpm for 1 min. The film was then immediately transferred into a nitrogen atmosphere and was illuminated by the focused UV beam at room temperature for 25 min for cross-linking. The composite membranes were then tailored into appropriate sections for further experiments.

Structural Characterizations. The liquid-crystal birefringence textures were analyzed using a Zeiss Axiovert 200 M inverted microscope. Corresponding polarized light images were captured from a CCD camera connected to a computer. For imaging, the domain textures from the lyotropic mesophase were annealed through heating and slow cooling protocols to develop typical liquid-crystal textures for characterization.

X-ray spectra were collected in the Dual Source and Environmental X-ray Scattering facility operated by the Laboratory for Research on the Structure of Matter at the University of Pennsylvania, using a Xeuss 2.0 system (Xenocs). The GeniX3D Cu source provides a wavelength of λ = 1.54 Å. A consistent sample to detector distance of 55 cm covering a range of accessible scattering vectors (q) from 0.016 to 1.02 Å^{-1} was maintained, and the 2-D scattering patterns were acquired with the line-eraser mode. Corresponding scattering patterns were azimuthally integrated into 1-D plots using the Foxtrot software package for scattering intensity (I) *versus* q, where $q = 4\pi \sin(\theta)/\lambda$ and the scattering angle is 2θ. Silver behenate was used as a calibration standard. For transmission scattering experiments, samples were packed between Kapton windows. In the case of GISAXS experiments, silicon substrates (with both bare SiO_2 and PVP-treated surface) were mounted on a standard GISAXS holder with an incidence angle between the substrate surface to the X-ray maintained from 0.15° to 0.2°. It should be noted that the characteristic $q_z' \gg q_c$ (~0.01 Å^{-1}), where the q_z' is the perpendicular q projection and the q_c is the q corresponding to the critical angle. As such, the 1-D plots from the 2-D GISAXS pattern were integrated by estimating $q_z' \sim q_z$.

A JEOL 7500F field-emission scanning electron microscope (HR-SEM) was utilized to characterize the nanoscale morphology of the cross-linked composite membranes and their supports. The surface characterization was based on sectioning vacuum-dried samples into 10 mm × 10 mm pieces. In order to prepare samples for cross-sectional imaging, dried samples were immediately cryo-fractured after submerging sections in a bath of liquid nitrogen for ~20 s. Samples were mounted on standard pin-stubs using carbon tape and were subsequently sputter-coated with ~3.0 nm of iridium, then loaded into the SEM chamber. Micrographs were photographed at a working distance of 8.0 mm with a consistent accelerating voltage of 10 kV.

A height-profile analysis of the silicon substrate supported H_I thin film was performed using a Bruker Dimension Icon AFM at the tapping mode with a MikroMasch HQ:NSC15/AL BS probe. In addition, mechanical characterization based on a TA Instrument ARES-G2 rheometer measured the toughness of the cross-linked H_I material. Specifically, cross-linked rectangular samples in the bulk were clamped to a tensile attachment loaded on the rheometer. The clamp pressure was sufficiently high to hold the samples in place without deforming the original conformation. The tensile force was measured over time as the samples were vertically strained along the longitudinal direction, at a rate $\dot{\gamma}$ = 0.001 s^{-1} until the samples failed.

Transport Characterizations. The thin-film composite H_I membranes were transferred into a 50 mL Millipore Amicon stirred cell (UFSC05001) situated in the lab with room temperature between 15 and 18 °C. The composite membrane was oriented with the surface layer facing the feed solution and was supported by a 4.5-cm-diameter PP/PE nonwoven mat. A customized stainless-steel disk with a circular opening was used to confine a controlled filtration area, corresponding to an active surface area of 2.4 cm^2 available for solvent permeation. In order to characterize the intrinsic transport properties of the membranes, compressed nitrogen gas with a well-regulated transmembrane pressure ranging from 1 to 80 psi was used to drive the solute rejection and hydraulic permeance characterization experiments. Note the maximum transmembrane hydraulic pressure for the H_I membranes was determined as ~400 psi using an HP4750 high-pressure stirred cell coupled with a 25-mm-area reducer. Before starting the solute rejection experiments, the H_I thin-film composites were rinsed thoroughly within the stirred cell to remove the sacrificial layer. The membranes were permeated with DI water for ~7 h. To provide a well-defined starting point for subsequent characterizations that involve comparisons of salt rejection experiments with Cl^- ions, membranes were then permeated with 10 mM NaCl for an additional 1 h to avoid potential complications associated with transient ion exchange. The membranes were continuously permeated with DI water and 10 mM NaCl solution for ~8 h before starting to collect specific permeate solutions. The solution permeated from the membrane was collected in a capped glass container or a polypropylene Falcon tube (for cationic dye solutions) situated on an electronic balance.

The MWCO experiments were conducted using molecules with known sizes to characterize the size-selective solute separation performance. A range of solutes with the geometric mean diameters ranging from ~0.4 to 4 nm was chosen to challenge the H_I composite membrane. As such, a series of small molecules of vitamin B12 (VB12), beta-cyclodextrin, alpha-cyclodextrin, vitamin B2 (VB2), and resorcinol were coupled with PEG (Polymer Source, Inc.) standards with number-averaged molecular weights of 0.60, 1.1, 2.0, and 4.0 kg mol^{-1} and polydispersity values of 1.1 or less. DI water with a pH of ~5.5 was stored in a polypropylene bottle before use. In order to prepare small-molecule feed solutions, solutes were dissolved in DI water at a concentration of 0.1 mM. Meanwhile, the PEG feed solutions were formulated with 1 g L^{-1} polymer in DI water. Similarly, dye rejection experiments were performed by permeating 0.1 mM solutions of Alcian blue (AB), rhodamine 6G (R6G), crystal violet (CV), Rose Bengal (RB), methyl orange (MO), and methylene blue (MB) that were dissolved in DI water through the membrane. During these solute rejection experiments, the single-species solute solution was permeated through the membrane bearing hydraulic flux at ~18 L m^{-2} h^{-1}, with the cell stirred at 400 rpm to reduce the concentration polarization. At least 5 mL of feed solution was permeated through the membrane from every single rejection experiment. It should be noted that no significant molecular fouling (*i.e.*, reduction in hydraulic permeance or irreversible dye deposition on the membrane) was observed during the rejection experiments.

The concentration of the permeate solution was analyzed by a Cary 100 ultraviolet−visible (UV−vis) spectrometer that calculates the concentration of the analyte using Beer−Lambert's law. A modified Dragendorff reagent method was used for the quantitative determination of the PEG solution concentration with a minimum coefficient of determination of >99% in calibration using linear regression.[70]

The single-salt rejection experiment was performed in two parts, in which a consistent ionic strength salt screening assay and an ionic strength dependent rejection were investigated in detail. In the first portion of the assay experiment, the rejection assay involved a series of single-salt solutions containing $CaCl_2$, $MgCl_2$, Na_2SO_4, $MgSO_4$, KCl, NaCl, and LiCl prepared with a consistent ionic strength 10 mM with the solution pH unadjusted. Meanwhile, additional single-salt

https://doi.org/10.1021/acsnano.1c00722
ACS Nano XXXX, XXX, XXX−XXX

$MgCl_2$ and NaCl solutions were prepared in a range of concentrations (by weight) ranging from 50 to 6000 ppm for the ionic strength dependent salt rejection experiment. In both parts, compressed-nitrogen-driven salt solution flow permeated through the membrane at a constant transmembrane pressure of 80 psi, with the cell stirred at 400 rpm. At least 8 mL of permeate solution was collected from every single-salt rejection experiment, and the salt concentration of the permeate was compared to the feed to calculate the percent rejection. Between salt rejection experiments, membranes were rinsed thoroughly with DI water for three times, and the dead-volume within the cell was subsequently flushed with ~3 mL of DI water. An Oakton Con 11 conductivity meter was used to assess the salt concentrations.

In order to compare the performance of H_I with other commercially available nanofiltration membranes, flat-sheet nanofiltration membranes purchased from the vendor were packed within the same stirred cell filtration setup as described above. A series of different nanofiltration membranes, including Filmtech polyamide NF270, Filmtech polyamide NF90, Synder polyamide NFG, Trisep cellulose acetate SB90, and Microdyn Nadir poly(ether sulfone) NP030, were investigated in detail. Membranes were rinsed with DI water for ~8 h prior to starting the salt rejection experiment using 200 ppm of NaCl and $MgCl_2$ as model salts. The salt rejection experiment utilized the same protocol as described above.

ASSOCIATED CONTENT

Supporting Information

The Supporting Information is available free of charge at https://pubs.acs.org/doi/10.1021/acsnano.1c00722.

The calculation for transport characterization, the calculation for pore dimension, the calculation for theoretical hydraulic permeability, NMR of AETDAB monomer, FTIR spectra of polymerization, stress−strain curve of polymerized film, POM images, schematic for geometrical dimensions, SAXS pattern of bulk film, 1D SAXS data, SEM micrographs of the support membranes, pure water flux as a function of transmembrane pressure, and schematic of solutes in the transport experiment (PDF)

AUTHOR INFORMATION

Corresponding Author

Chinedum O. Osuji − *Department of Chemical and Biomolecular Engineering, University of Pennsylvania, Philadelphia, Pennsylvania 19104, United States;* orcid.org/0000-0003-0261-3065; Email: cosuji@seas.upenn.edu

Authors

Yizhou Zhang − *Department of Chemical and Biomolecular Engineering, University of Pennsylvania, Philadelphia, Pennsylvania 19104, United States*

Ruiqi Dong − *Department of Chemical and Biomolecular Engineering, University of Pennsylvania, Philadelphia, Pennsylvania 19104, United States*

Uri R. Gabinet − *Department of Chemical and Biomolecular Engineering, University of Pennsylvania, Philadelphia, Pennsylvania 19104, United States*

Ryan Poling-Skutvik − *Department of Chemical and Biomolecular Engineering, University of Pennsylvania, Philadelphia, Pennsylvania 19104, United States;* orcid.org/0000-0002-1614-1647

Na Kyung Kim − *Department of Chemical and Biomolecular Engineering, University of Pennsylvania, Philadelphia, Pennsylvania 19104, United States*

Changyeon Lee − *Department of Chemical and Biomolecular Engineering, University of Pennsylvania, Philadelphia, Pennsylvania 19104, United States*

Omar Q. Imran − *Department of Chemical and Biomolecular Engineering, University of Pennsylvania, Philadelphia, Pennsylvania 19104, United States;* orcid.org/0000-0002-6166-1246

Xunda Feng − *Center for Advanced Low-dimension Materials, State Key Laboratory for Modification of Chemical Fibers and Polymer Materials, Donghua University, Shanghai 201620, China;* orcid.org/0000-0002-4528-0769

Complete contact information is available at: https://pubs.acs.org/10.1021/acsnano.1c00722

Notes

The authors declare no competing financial interest.

ACKNOWLEDGMENTS

Portions of this work were made possible with support from the NSF through PFI:AIR-TT IIP-1640375 and CBET1703494. Facilities use was supported by the Singh Center for Nanotechnology at the University of Pennsylvania, and the Dual Source and Environmental X-ray scattering facility operated by the Laboratory for Research on the Structure of Matter at the University of Pennsylvania which is funded in part by NSF MRSEC 17-20530. The equipment purchase was made possible by a NSF MRI grant (17-25969), a ARO DURIP grant (W911NF-17-1-0282), and the University of Pennsylvania. C.O.O. acknowledges additional financial support from the NSF (DMR-1945966). The authors also thank Professor Paul A. Heiney from the Department of Physics and Astronomy, University of Pennsylvania, and Professor William A. Phillip from the Department of Chemical and Biomolecular Engineering, University of Notre Dame, for helpful discussions.

REFERENCES

(1) Van der Bruggen, B.; Vandecasteele, C. Removal of Pollutants from Surface Water and Groundwater by Nanofiltration: Overview of Possible Applications in the Drinking Water Industry. *Environ. Pollut.* **2003**, *122*, 435−445.

(2) Butkovskyi, A.; Bruning, H.; Kools, S. A.; Rijnaarts, H. H.; Van Wezel, A. P. Organic Pollutants in Shale Gas Flowback and Produced Waters: Identification, Potential Ecological Impact, and Implications for Treatment Strategies. *Environ. Sci. Technol.* **2017**, *51*, 4740−4754.

(3) Steinle-Darling, E.; Reinhard, M. Nanofiltration for Trace Organic Contaminant Removal: Structure, Solution, and Membrane Fouling Effects on the Rejection of Perfluorochemicals. *Environ. Sci. Technol.* **2008**, *42*, 5292−5297.

(4) Mohammad, A. W.; Teow, Y. H.; Ang, W. L.; Chung, Y. T.; Oatley-Radcliffe, D. L.; Hilal, N. Nanofiltration Membranes Review: Recent Advances and Future Prospects. *Desalination* **2015**, *356*, 226−254.

(5) Fane, A. G.; Wang, R.; Hu, M. X. Synthetic Membranes for Water Purification: Status and Future. *Angew. Chem., Int. Ed.* **2015**, *54*, 3368−3386.

(6) Werber, J. R.; Osuji, C. O.; Elimelech, M. Materials for Next-Generation Desalination and Water Purification Membranes. *Nat. Rev. Mater.* **2016**, *1*, 16018.

(7) Lau, W. J.; Ismail, A. F.; Misdan, N.; Kassim, M. A. A Recent Progress in Thin Film Composite Membrane: A Review. *Desalination* **2012**, *287*, 190−199.

(8) Loeb, S.; Sourirajan, S. Sea Water Demineralization by Means of an Osmotic Membrane. *Adv. Chem. Ser.* **1963**, *38*, 117−132.

(9) Hołda, A. K.; Vankelecom, I. F. Understanding and Guiding the Phase Inversion Process for Synthesis of Solvent Resistant Nanofiltration Membranes. *J. Appl. Polym. Sci.* **2015**, *132*, 42130.
(10) Freger, V. Nanoscale Heterogeneity of Polyamide Membranes Formed by Interfacial Polymerization. *Langmuir* **2003**, *19*, 4791−4797.
(11) Liang, Y.; Zhu, Y.; Liu, C.; Lee, K.-R.; Hung, W.-S.; Wang, Z.; Li, Y.; Elimelech, M.; Jin, J.; Lin, S. Polyamide Nanofiltration Membrane with Highly Uniform Sub-Nanometre Pores for Sub-1 Å Precision Separation. *Nat. Commun.* **2020**, *11*, 2015.
(12) Bowen, W. R.; Welfoot, J. S. Modelling of Membrane Nanofiltration—Pore Size Distribution Effects. *Chem. Eng. Sci.* **2002**, *57*, 1393−1407.
(13) Mehta, A.; Zydney, A. L. Permeability and Selectivity Analysis for Ultrafiltration Membranes. *J. Membr. Sci.* **2005**, *249*, 245−249.
(14) Park, H. B.; Kamcev, J.; Robeson, L. M.; Elimelech, M.; Freeman, B. D. Maximizing the Right Stuff: The Trade-Off between Membrane Permeability and Selectivity. *Science* **2017**, *356*, 1137.
(15) Gin, D. L.; Noble, R. D. Designing the Next Generation of Chemical Separation Membranes. *Science* **2011**, *332*, 674−676.
(16) Hou, J.; Zhang, H.; Simon, G. P.; Wang, H. Polycrystalline Advanced Microporous Framework Membranes for Efficient Separation of Small Molecules and Ions. *Adv. Mater.* **2020**, *32*, 1902009.
(17) Koros, W. J.; Zhang, C. Materials for Next-Generation Molecularly Selective Synthetic Membranes. *Nat. Mater.* **2017**, *16*, 289−297.
(18) Li, Y.; Wu, Q.; Guo, X.; Zhang, M.; Chen, B.; Wei, G.; Li, X.; Li, X.; Li, S.; Ma, L. Laminated Self-Standing Covalent Organic Framework Membrane with Uniformly Distributed Subnanopores for Ionic and Molecular Sieving. *Nat. Commun.* **2020**, *11*, 599.
(19) Fan, H.; Gu, J.; Meng, H.; Knebel, A.; Caro, J. High-Flux Membranes Based on the Covalent Organic Framework COF-LZU1 for Selective Dye Separation by Nanofiltration. *Angew. Chem., Int. Ed.* **2018**, *57*, 4083−4087.
(20) Liu, X.; Demir, N. K.; Wu, Z.; Li, K. Highly Water-Stable Zirconium Metal−Organic Framework Uio-66 Membranes Supported on Alumina Hollow Fibers for Desalination. *J. Am. Chem. Soc.* **2015**, *137*, 6999−7002.
(21) Denny, M. S.; Moreton, J. C.; Benz, L.; Cohen, S. M. Metal−Organic Frameworks for Membrane-Based Separations. *Nat. Rev. Mater.* **2016**, *1*, 16078.
(22) Jimenez-Solomon, M. F.; Song, Q.; Jelfs, K. E.; Munoz-Ibanez, M.; Livingston, A. G. Polymer Nanofilms with Enhanced Microporosity by Interfacial Polymerization. *Nat. Mater.* **2016**, *15*, 760−767.
(23) McKeown, N. B.; Budd, P. M. Exploitation of Intrinsic Microporosity in Polymer-Based Materials. *Macromolecules* **2010**, *43*, 5163−5176.
(24) Hummer, G.; Rasaiah, J. C.; Noworyta, J. P. Water Conduction through the Hydrophobic Channel of a Carbon Nanotube. *Nature* **2001**, *414*, 188−190.
(25) Fornasiero, F.; Park, H. G.; Holt, J. K.; Stadermann, M.; Grigoropoulos, C. P.; Noy, A.; Bakajin, O. Ion Exclusion by Sub-2-Nm Carbon Nanotube Pores. *Proc. Natl. Acad. Sci. U. S. A.* **2008**, *105*, 17250−17255.
(26) Shen, Y.-x.; Song, W.; Barden, D. R.; Ren, T.; Lang, C.; Feroz, H.; Henderson, C. B.; Saboe, P. O.; Tsai, D.; Yan, H.; Butler, P. J.; Bazan, G. C.; Phillip, W. A.; Hickey, R. J.; Cremer, P. S.; Vashisth, H.; Kumar, M. Achieving High Permeability and Enhanced Selectivity for Angstrom-Scale Separations Using Artificial Water Channel Membranes. *Nat. Commun.* **2018**, *9*, 2294.
(27) Song, W.; Joshi, H.; Chowdhury, R.; Najem, J. S.; Shen, Y.-x.; Lang, C.; Henderson, C. B.; Tu, Y.-M.; Farell, M.; Pitz, M. E.; Maranas, C. D.; Cremer, P. S.; Hickey, R. J.; Sarles, S. A.; Hou, J.-l.; Aksimentiev, A.; Kumar, M. Artificial Water Channels Enable Fast and Selective Water Permeation through Water-Wire Networks. *Nat. Nanotechnol.* **2020**, *15*, 73−79.
(28) Yang, Q.; Su, Y.; Chi, C.; Cherian, C.; Huang, K.; Kravets, V. G.; Wang, F. C.; Zhang, J. C.; Pratt, A.; Grigorenko, A. N.; Nair, R. R. Ultrathin Graphene-Based Membrane with Precise Molecular Sieving and Ultrafast Solvent Permeation. *Nat. Mater.* **2017**, *16*, 1198−1202.
(29) Chen, L.; Shi, G.; Shen, J.; Peng, B.; Zhang, B.; Wang, Y.; Bian, F.; Wang, J.; Li, D.; Qian, Z.; Xu, G.; Liu, G.; Zeng, J.; Zhang, L.; Yang, Y.; Zhou, G.; Wu, M.; Jin, W.; Li, J.; Fang, H. Ion Sieving in Graphene Oxide Membranes *Via* Cationic Control of Interlayer Spacing. *Nature* **2017**, *550*, 380−383.
(30) Feng, X.; Kawabata, K.; Cowan, M. G.; Dwulet, G. E.; Toth, K.; Sixdenier, L.; Haji-Akbari, A.; Noble, R. D.; Elimelech, M.; Gin, D. L.; Osuji, C. O. Single Crystal Texture by Directed Molecular Self-Assembly Along Dual Axes. *Nat. Mater.* **2019**, *18*, 1235−1243.
(31) Feng, X.; Tousley, M. E.; Cowan, M. G.; Wiesenauer, B. R.; Nejati, S.; Choo, Y.; Noble, R. D.; Elimelech, M.; Gin, D. L.; Osuji, C. O. Scalable Fabrication of Polymer Membranes with Vertically Aligned 1 nm Pores by Magnetic Field Directed Self-Assembly. *ACS Nano* **2014**, *8*, 11977−11986.
(32) Zhou, M.; Kidd, T. J.; Noble, R. D.; Gin, D. L. Supported Lyotropic Liquid-Crystal Polymer Membranes: Promising Materials for Molecular-Size-Selective Aqueous Nanofiltration. *Adv. Mater.* **2005**, *17*, 1850−1853.
(33) Lugger, J. A.; Mulder, D. J.; Bhattacharjee, S.; Sijbesma, R. P. Homeotropic Self-Alignment of Discotic Liquid Crystals for Nanoporous Polymer Films. *ACS Nano* **2018**, *12*, 6714−6724.
(34) Feng, X.; Imran, Q.; Zhang, Y.; Sixdenier, L.; Lu, X.; Kaufman, G.; Gabinet, U.; Kawabata, K.; Elimelech, M.; Osuji, C. O. Precise Nanofiltration in a Fouling-Resistant Self-Assembled Membrane with Water-Continuous Transport Pathways. *Sci. Adv.* **2019**, *5*, No. eaav9308.
(35) Zhou, M.; Nemade, P. R.; Lu, X.; Zeng, X.; Hatakeyama, E. S.; Noble, R. D.; Gin, D. L. New Type of Membrane Material for Water Desalination Based on a Cross-Linked Bicontinuous Cubic Lyotropic Liquid Crystal Assembly. *J. Am. Chem. Soc.* **2007**, *129*, 9574−9575.
(36) Carter, B. M.; Wiesenauer, B. R.; Hatakeyama, E. S.; Barton, J. L.; Noble, R. D.; Gin, D. L. Glycerol-Based Bicontinuous Cubic Lyotropic Liquid Crystal Monomer System for the Fabrication of Thin-Film Membranes with Uniform Nanopores. *Chem. Mater.* **2012**, *24*, 4005−4007.
(37) Karan, S.; Jiang, Z.; Livingston, A. G. Sub−10 nm Polyamide Nanofilms with Ultrafast Solvent Transport for Molecular Separation. *Science* **2015**, *348*, 1347−1351.
(38) Chowdhury, M. R.; Steffes, J.; Huey, B. D.; McCutcheon, J. R. 3D Printed Polyamide Membranes for Desalination. *Science* **2018**, *361*, 682−686.
(39) Zodrow, K. R.; Li, Q.; Buono, R. M.; Chen, W.; Daigger, G.; Dueñas-Osorio, L.; Elimelech, M.; Huang, X.; Jiang, G.; Kim, J.-H.; Logan, B. E.; Sedlak, D. L.; Westerhoff, P.; Alvarez, P. J. J. Advanced Materials, Technologies, and Complex Systems Analyses: Emerging Opportunities to Enhance Urban Water Security. *Environ. Sci. Technol.* **2017**, *51*, 10274−10281.
(40) Eugene, E. A.; Phillip, W. A.; Dowling, A. W. Data Science-Enabled Molecular-to-Systems Engineering for Sustainable Water Treatment. *Curr. Opin. Chem. Eng.* **2019**, *26*, 122−130.
(41) Kato, T.; Uchida, J.; Ichikawa, T.; Sakamoto, T. Functional Liquid Crystals Towards the Next Generation of Materials. *Angew. Chem., Int. Ed.* **2018**, *57*, 4355−4371.
(42) Gin, D. L.; Lu, X.; Nemade, P. R.; Pecinovsky, C. S.; Xu, Y.; Zhou, M. Recent Advances in the Design of Polymerizable Lyotropic Liquid-Crystal Assemblies for Heterogeneous Catalysis and Selective Separations. *Adv. Funct. Mater.* **2006**, *16*, 865−878.
(43) Sakamoto, T.; Ogawa, T.; Nada, H.; Nakatsuji, K.; Mitani, M.; Soberats, B.; Kawata, K.; Yoshio, M.; Tomioka, H.; Sasaki, T.; Kimura, M.; Henmi, M.; Kato, T. Development of Nanostructured Water Treatment Membranes Based on Thermotropic Liquid Crystals: Molecular Design of Sub-Nanoporous Materials. *Adv. Sci.* **2018**, *5*, 1700405.
(44) Boussu, K.; Zhang, Y.; Cocquyt, J.; Van der Meeren, P.; Volodin, A.; Van Haesendonck, C.; Martens, J.; Van der Bruggen, B. Characterization of Polymeric Nanofiltration Membranes for System-

https://doi.org/10.1021/acsnano.1c00722
ACS Nano XXXX, XXX, XXX−XXX

atic Analysis of Membrane Performance. *J. Membr. Sci.* **2006**, *278*, 418−427.
(45) Tousley, M. E.; Feng, X.; Elimelech, M.; Osuji, C. O. Aligned Nanostructured Polymers by Magnetic-Field-Directed Self-Assembly of a Polymerizable Lyotropic Mesophase. *ACS Appl. Mater. Interfaces* **2014**, *6*, 19710−19717.
(46) Mauter, M. S.; Elimelech, M.; Osuji, C. O. Stable Sequestration of Single-Walled Carbon Nanotubes in Self-Assembled Aqueous Nanopores. *J. Am. Chem. Soc.* **2012**, *134*, 3950−3953.
(47) Mauter, M. S.; Elimelech, M.; Osuji, C. O. Nanocomposites of Vertically Aligned Single-Walled Carbon Nanotubes by Magnetic Alignment and Polymerization of a Lyotropic Precursor. *ACS Nano* **2010**, *4*, 6651−6658.
(48) Tomita, S.; Urakawa, H.; Wataoka, I.; Sasaki, S.; Sakurai, S. Complete and Comprehensive Orientation of Cylindrical Microdomains in a Block Copolymer Sheet. *Polym. J.* **2016**, *48*, 1123−1131.
(49) Villar, M. A.; Rueda, D. R.; Ania, F.; Thomas, E. L. Study of Oriented Block Copolymers Films Obtained by Roll-Casting. *Polymer* **2002**, *43*, 5139−5145.
(50) Asghar, K. A.; Elliott, J. M.; Squires, A. M. 2D Hexagonal Mesoporous Platinum Films Exhibiting Biaxial, in-Plane Pore Alignment. *J. Mater. Chem.* **2012**, *22*, 13311−13317.
(51) Sobera, M.; Kleijn, C. Hydraulic Permeability of Ordered and Disordered Single-Layer Arrays of Cylinders. *Phys. Rev. E* **2006**, *74*, 036301.
(52) Faraone, A.; Magazu, S.; Maisano, G.; Migliardo, P.; Tettamanti, E.; Villari, V. The Puzzle of Poly(Ethylene Oxide) Aggregation in Water: Experimental Findings. *J. Chem. Phys.* **1999**, *110*, 1801−1806.
(53) Meireles, M.; Bessieres, A.; Rogissart, I.; Aimar, P.; Sanchez, V. An Appropriate Molecular Size Parameter for Porous Membranes Calibration. *J. Membr. Sci.* **1995**, *103*, 105−115.
(54) Shao, J.; Baltus, R. E. Hindered Diffusion of Dextran and Polyethylene Glycol in Porous Membranes. *AIChE J.* **2000**, *46*, 1149−1156.
(55) Zhang, J.; Ma, P. X. Cyclodextrin-Based Supramolecular Systems for Drug Delivery: Recent Progress and Future Perspective. *Adv. Drug Delivery Rev.* **2013**, *65*, 1215−1233.
(56) Zeman, L. J.; Zydney, A. *Microfiltration and Ultrafiltration: Principles and Applications*; Marcel Dekker: New York, 1996.
(57) Barhate, R. S.; Ramakrishna, S. Nanofibrous Filtering Media: Filtration Problems and Solutions from Tiny Materials. *J. Membr. Sci.* **2007**, *296*, 1−8.
(58) Kanani, D. M.; Fissell, W. H.; Roy, S.; Dubnisheva, A.; Fleischman, A.; Zydney, A. L. Permeability−Selectivity Analysis for Ultrafiltration: Effect of Pore Geometry. *J. Membr. Sci.* **2010**, *349*, 405−410.
(59) Feinberg, B. J.; Hsiao, J. C.; Park, J.; Zydney, A. L.; Fissell, W. H.; Roy, S. Slit Pores Preferred over Cylindrical Pores for High Selectivity in Biomolecular Filtration. *J. Colloid Interface Sci.* **2018**, *517*, 176−181.
(60) Conway, B. E. *Ionic Hydration in Chemistry and Biophysics*; Elsevier: Amsterdam, 1981; Vol. *741*.
(61) Bhattacharyya, D.; McCarthy, J.; Grives, R. Charged Membrabe Ultrafiltration of Inorganic Ions in Single Annd Multi-Salt Systems. *AIChE J.* **1974**, *20*, 1206−1212.
(62) Bhattacharyya, D.; Garrison, K.; Jumawan, A., Jr; Grieves, R. Membrane Ultrafiltration of a Nonionic Surfactant and Inorganic Salts from Complex Aqueous Suspensions: Design for Water Reuse. *AIChE J.* **1975**, *21*, 1057−1065.
(63) Barry, E.; McBride, S. P.; Jaeger, H. M.; Lin, X.-M. Ion Transport Controlled by Nanoparticle-Functionalized Membranes. *Nat. Commun.* **2014**, *5*, 5847.
(64) Zhang, M.; Guan, K.; Ji, Y.; Liu, G.; Jin, W.; Xu, N. Controllable Ion Transport by Surface-Charged Graphene Oxide Membrane. *Nat. Commun.* **2019**, *10*, 1253.
(65) Zhang, Y.; Mulvenna, R. A.; Qu, S.; Boudouris, B. W.; Phillip, W. A. Block Polymer Membranes Functionalized with Nanoconfined Polyelectrolyte Brushes Achieve Sub-Nanometer Selectivity. *ACS Macro Lett.* **2017**, *6*, 726−732.
(66) Burns, D. B.; Zydney, A. L. Contributions to Electrostatic Interactions on Protein Transport in Membrane Systems. *AIChE J.* **2001**, *47*, 1101−1114.
(67) Argyris, D.; Cole, D. R.; Striolo, A. Ion-Specific Effects under Confinement: The Role of Interfacial Water. *ACS Nano* **2010**, *4*, 2035−2042.
(68) Yu, M.; Funke, H. H.; Falconer, J. L.; Noble, R. D. Gated Ion Transport through Dense Carbon Nanotube Membranes. *J. Am. Chem. Soc.* **2010**, *132*, 8285−8290.
(69) Secchi, E.; Niguès, A.; Jubin, L.; Siria, A.; Bocquet, L. Scaling Behavior for Ionic Transport and Its Fluctuations in Individual Carbon Nanotubes. *Phys. Rev. Lett.* **2016**, *116*, 154501.
(70) Jia, Z.; Tian, C. Quantitative Determination of Polyethylene Glycol with Modified Dragendorff Reagent Method. *Desalination* **2009**, *247*, 423−429.

https://doi.org/10.1021/acsnano.1c00722
ACS Nano XXXX, XXX, XXX−XXX